PCCP

ARTICLE

Formation and Nitrile Hydrogenation Performance of Ru Nanoparticles on a K-doped Al₂O₃ Surface

Satoshi Muratsugu,[a,b,c] Sutasinee Kityakarn,[a,d,e] Fei Wang,[b,c] Nozomu Ishiguro,[d] Takashi Kamachi,[f] Kazunari Yoshizawa,[f] Oki Sekizawa,[g] Tomoya Uruga,[g, h] and Mizuki Tada[a,b,c,d*]

Decarbonylation-promoted Ru nanoparticle formation from Ru₃(CO)₁₂ on a basic K-doped Al₂O₃ surface was investigated by *in situ* FT-IR and *in situ* XAFS. Supported Ru₃(CO)₁₂ clusters on K-doped Al₂O₃ were converted stepwise to Ru nanoparticles, which catalyzed the selective hydrogenation of nitriles to the corresponding primary amines via initial decarbonylation, the nucleation of the Ru cluster core, and the growth of metallic Ru nanoparticles on the surface. As a result, small Ru nanoparticles, with an average diameter of less than 2 nm, were formed on the support and acted as efficient catalysts for nitrile hydrogenation at 343 K under hydrogen at atmospheric pressure. The structure and catalytic performance of Ru catalysts depended strongly on the type of oxide support, and the K-doped Al₂O₃ support acted as a good oxide for the selective nitrile hydrogenation without basic additives like ammonia. The activation of nitriles on the modelled Ru catalyst was also investigated by DFT calculations, and the adsorption structure of a nitrene-like intermediate, which was favourable for high primary amine selectivity, was the most stable structure on Ru compared with other intermediate structures.

[a] Institute for Molecular Science, 38 Nishigo-naka, Myodaiji, Okazaki, Aichi 444-8585, Japan.

[b] The Graduate University for Advanced Studies (SOKENDAI), 38 Nishigo-naka, Myodaiji, Okazaki, Aichi 444-8585, Japan.

[c] Department of Chemistry, Graduate School of Science, Nagoya University, Furo, Chikusa, Nagoya, Aichi 464-8602, Japan.

[d] Research Center for Materials Science, Nagoya University, Furo, Chikusa, Nagoya, Aichi 464-8602, Japan.

[e] Department of Chemistry, Faculty of Science, Kasetsart University, Bangkok 10903, Thailand.

[f] Institute for Materials Chemistry and Engineering and International Research Center for Molecular Systems, Kyushu University, Fukuoka 819-0395, Japan.

[g] Innovation Research Center for Fuel Cells, University of Electro-Communications, 1-5-1 Chofu, Tokyo 182-8585, Japan.

[h] Japan Synchrotron Radiation Research Institute, SPring-8, 1-1-1 Koto, Sayo, Hyogo 679-5198, Japan.

* Fax: +81-52-788-6200; E-mail: mtada@chem.nagoya-u.ac.jp

† Electronic Supplementary Information (ESI) available: [the setup of *in situ* QXAFS, Ru K-edge XAFS spectra, CO adsorption isotherms, XRD patterns, and DFT calculations are summarized]. See DOI: XXXXXXXX

1. Introduction

Amines, particularly lower aliphatic amines, are important for industry, in areas such as chemical production, pharmaceuticals, polymer production, textiles, and rubber. Reductive amination of aldehydes and ketones and hydrogenation of nitriles are well-known amine preparation methods.[1-8] Selectivity for primary amines is a crucial problem in the preparation of amines because of the facile formation of secondary and tertiary amines under the reaction conditions. The addition of ammonia or base additives is a typical method for reducing these unfavorable intermediates, and improvements of primary amine selectivity have been reported for catalysts including [RuCl₂(PPh₃)₃],[9-10] M/NaY and M-Ni/NaY (M: Ru, Rh, Pd, and Pt),[11] Raney Ni, and Co[12-13] etc.

Selective hydrogenation catalysts for primary amines that do not require ammonia are particularly attractive. There are several reports of nitrile hydrogenation in liquid phases without ammonia or basic additives.[14-24] Several transition metals, for example, Co, Ni, Ru, Rh, Cu, Pd, and Pt, have been

investigated as active catalysts for nitrile hydrogenation. Co, Ni, and Ru tend to be selective for primary amines,[15-16, 18, 20-38] whereas Cu and Rh are selective for secondary amines,[15, 22] and Pd and Pt are selective for tertiary amines.[21, 27, 38-40] Several Ru complexes are selective catalysts for nitrile hydrogenation to primary amines, including $Ru(cod)(methylallyl)_2$ (cod = 1,5-cyclooctadiene) and imidazolylphosphine ligand systems,[30] $Ru(\eta^6-C_6H_6)\{(XyN-o-C_6H_4)_2S\}$ (Xy = $3,5-Me_2C_6H_3$) and PCy_3 (Cy = cyclohexyl) ligand systems[31] and $RuH_2(\eta^2-H_2)_2(PCyp_3)_2$ (Cyp = cyclopentyl).[33] Segobia et al. reported that transition metals (Ni, Co, Ru, Cu, Pd, and Pt) supported on silica catalyzed the hydrogenation of n-butyronitrile to n-butylamine at 373 K under 13 bar of H_2. The n-butylamine selectivity was in the order Ni > Co > Ru > Pt, and Ru predominately produced n-butylamine with traces of secondary amine and secondary imines.[15] Huang and Sachtler reported selective n-butylamine formation on Ru-supported NaY (Ru/NaY: 67.9% at 89.2% conversion and Ru-Ni/NaY: 61.8% at 100% conversion), and the selectivity significantly increased in the presence of ammonia (Ru-Ni/NaY: 91.5% at 87.1% conversion).[11] These catalysts have also been used for the secondary and tertiary amine synthesis by the N-alkylation of ammonia and related compounds with alcohol on a $[Ru(p-cymene)Cl_2]_2$ and dppf (= 1,1'-bis(diphenylphosphino)ferrocene) ligand system,[41] and $Ru(OH)_x$ supported oxide catalysts;[42-44] the synthesis of amides on $RuCl_2(\eta^6-C_6Me_6)\{P(NMe_2)_3\}$,[45] cis-$Ru(acac)_2(PPh_2py)_2$, (acac = acetylacetonato, PPh_2py = diphenyl-2-pyridylphosphine),[46] and $Ru(OH)_x/Al_2O_3$;[47] the synthesis of nitriles on $RuH_2(PPh_3)_4$,[48] $RuH(bmpi)(PPh_3)_2$ (bmpi = 1,3-bis(6'-methyl-2'-pyridylimino)isoindoline),[49] Ru/Al_2O_3[50] and $Ru(OH)_x$ supported oxide catalysts;[51-55] the synthesis of aldimines[56] and the aerobic oxidation of alcohol on $Ru(OH)_x$ supported oxide catalysts,[54-55, 57-58] and the synthesis of alcohol on $Ru(OH)_x$ supported oxide catalysts.[54, 59-60]

In heterogeneous catalytic systems, the effect of supports on nitrile hydrogenation has been also investigated, and LiOH-modified/Al_2O_3,[23-24] nitrogen-doped carbon nanospheres,[29] Mg(Al)O,[61] K/$\gamma-Al_2O_3$,[62] TiO_2,[28, 63] MgO,[62-63] ThO_2,[63] and UO_2[63] showed high selectivity for primary amines in nitrile hydrogenation. Alkali metal ions enhance the basic properties of the support surfaces and often act as promoters for nitrile hydrogenation by polarizing the substrates through the electronic interactions between the alkali metal ions and metal catalysts/reactants.[23-24, 61-62] Basic supports also affect the structures of the supported metal species, such as their dispersion, particle size, and specific adsorption site.[2, 23-24, 61-65] Chojecki et al. reported the enhancement of the activity and selectivity of n-butyronitrile hydrogenation on Raney Co modified with LiOH, arising from the increase in the proportion of metallic surface sites and the decrease in adsorption sites for n-butylamine, which is an intermediate for by-product formation.[23-24] Also, Gluhoi et al. reported the influence of basic supports on the selectivity of acetonitrile hydrogenation on inorganic oxide-supported Ni catalysts.[63]

For supported Ru catalysts, differences in the structure of supported Ru species on inorganic oxides (V_2O_5, SiO_2, TiO_2,

Al_2O_3, K-doped Al_2O_3, and MgO), which directly affect their catalytic performance for CO hydrogenation, were investigated by temperature-programmed desorption, IR, and X-ray absorption fine structure (XAFS) spectroscopy.[64-65] Metallic Ru species, characterized by temperature-programmed reduction, X-ray diffraction (XRD), and transmission electron microscopy (TEM), are active and selective for primary amine formation through nitrile hydrogenation.[11, 15-16, 66] Ortiz-Cervantes et al. reported that 2-3 nm Ru nanoparticles stabilized by sodium dodecylsulfate etc., prepared by the thermal decomposition of $Ru_3(CO)_{12}$, yielded benzylamine for benzonitrile hydrogenation at 900 psi and 563 K (56.6% selectivity at 100% conversion).[66]

Here, we report Ru nanoparticle catalysts dispersed on a basic K-doped Al_2O_3 support surface, which were active and selective for nitrile hydrogenation to corresponding primary amines in the absence of ammonia. The local structures and reactivity of the supported Ru catalysts for the valeronitrile (pentanenitrile) hydrogenation depended strongly on the type of oxide support. A $Ru_3(CO)_{12}$ precursor was attached to the surface of the basic K-doped Al_2O_3 support by releasing its coordinating CO ligands and was converted stepwise to metallic Ru nanoparticles, which were efficient for selective nitrile hydrogenation. The formation of the active Ru nanoparticles was investigated by in situ FT-IR, in situ XAFS analysis, and the nitrile activation mechanism and DFT calculations.

2. Experimental and computational methods

2.1 Catalyst preparation

GENERAL PROCEDURE: All operations were performed under N_2 atmosphere (99.9%) by standard Schlenk tube techniques or in a glovebox. Chemicals were used without further purification unless otherwise noted, and solvents were dried by literature methods.[67] The solvents were passed over activated alumina and supported copper catalysts supplied by Nikko Hansen & Co., Ltd. All samples were stored under N_2 atmosphere after preparation and were used as catalysts without exposure to air.

SUPPORT PREPARATION AND PRETREATMENT: K-doped Al_2O_3 was prepared by impregnation of Aeroxide Alu C (Nippon Aerosil, surface area estimated by BET analysis: 98 m^2 g^{-1}) in an aqueous K_2CO_3 solution (K: 2, 4, or 6 wt %) using a method similar to a reported method.[64-65] The mixture was stirred at 293–298 K for 24 h and dried at 358 K for 48 h. The resulting powder was calcined at 773 K with a heating rate of 7.9 K min^{-1} for 3 h under air and evacuated under vacuum. Water vapor was exposed to the dried sample at 298 K for 30 min, referred to as K-Alu C (surface area: 88 m^2 g^{-1}). $\gamma-Al_2O_3$ (Soekawa, 99 m^2 g^{-1}) was impregnated with K_2CO_3 (K: 4 wt %) using a similar method, and K-$\gamma-Al_2O_3$ (surface area: 89 m^2 g^{-1}) was obtained.

Other oxide supports used were SiO_2 (Aerosil 200, Nippon Aerosil, surface area: 194 m^2 g^{-1}), ZnO (Wako Chemicals, 4 m^2 g^{-1}), TiO_2 (P-25, Degussa, 48 m^2 g^{-1}), $\alpha-Al_2O_3$ (Wako Chemicals, 5 m^2 g^{-1}), undoped $\gamma-Al_2O_3$, and undoped Alu C, and they were calcined at 573 K with a heating rate of 4.6 K

min⁻¹ for 3 h under air. MgO (Wako Chemicals, 31 m² g⁻¹) was calcined at 673 K with a heating rate of 6.3 K min⁻¹ for 3 h under air.

RU₃(CO)₁₂-IMPREGNATED CATALYSTS: Ru₃(CO)₁₂ (Aldrich, 99.9%) was purified by recrystallization in dehydrated *n*-hexane at 343 K under N₂ atmosphere. Purified Ru₃(CO)₁₂ was dissolved in dehydrated *n*-hexane (Wako Chemicals, 96.0%, 30 mL) at 343 K and impregnated with the pretreated oxide supports (1 g) for 30 min at 293–298 K under an N₂ atmosphere. The Ru loading was 1, 1.5, 2, 3, 4, 6, 8, or 10 wt % on K-Alu C (K: 4 wt%). The solvent was evaporated at 293–298 K and dried under vacuum for 30 min. Finally, the sample was heated under vacuum to 723 K (7.1 K min⁻¹) and kept at 723 K for 2 h, followed by treatment with H₂ (99.999%, 15 kPa) at 723 K for 1 h. The samples obtained after reduction with hydrogen at 723 K are referred to as Ru₃₋CO/K-Alu C. The impregnation of the other supports with Ru₃(CO)₁₂ was achieved by using a similar method, and the obtained samples are referred to as Ru₃₋CO/oxide support (Ru: 2 wt %). The surface area of Ru₃₋CO/K-Alu C (K: 4 wt%, Ru: 2 wt%) was observed to be 69 m² g⁻¹ by BET analysis.

RU(C₅H₇O₂)₃-IMPREGNATED CATALYST: K-Alu C (K: 4 wt %; 1 g) was impregnated with Ru(C₅H₇O₂)₃ (Aldrich, 97%; denoted as Ru(acac)₃) dissolved in dehydrated *n*-hexane (30 mL) at 293–298 K for 30 min. The Ru loading was 2 wt %. The solvent was evaporated under vacuum at 293–298 K and dried under vacuum for 30 min. The solid was reduced with hydrogen using a method similar to the one used to prepare Ru₃₋CO/K-Alu C from Ru₃(CO)₁₂. The sample after reduction with hydrogen at 723 K is referred to as Ru₋acac/K-Alu C.

2.2 Catalyst characterization

FOURIER-TRANSFORM INFRARED SPECTROSCOPY (FT-IR): *In situ* FT-IR spectra of Ru₃₋CO/K-Alu C were recorded on a JASCO FT/IR-6100 spectrometer with a resolution of 4 cm⁻¹. Diluted Ru₃₋CO/K-Alu C (37% Ru₃₋CO/K-Alu C (K: 4 wt %, Ru: 4 wt %) in K-Alu C; amount of the mixture: 70 mg) was pressed into a disk (20 mm in diameter) in a glovebox and placed in an *in situ* IR cell with two CaF₂ windows without exposure to air. The sample disk was evacuated for 5 min, and then an FT-IR spectrum was recorded. The temperature program increased from 298 to 723 K over 1 h (7.1 K min⁻¹) under vacuum, and *in situ* FT-IR spectra were recorded every 2 min during the heating process. Finally, the sample was kept at 723 K for 5 min, and an FT-IR spectrum was recorded.

The FT-IR spectra were analyzed by Igor Pro 6.3. The baseline of the observed spectra was subtracted with a linear curve, and peaks in an FT-IR spectrum were fitted with a linear combination of Gaussian curves. The peak area of each peak was calculated from the peak height multiplied by its FWHM. The initial number of coordinating carbonyl groups at 298 K was reported to be 11,[68-69] thus the numbers of carbonyl groups remaining on the Ru species were estimated by the following equation,

$$\text{Numbers of remained CO groups} = \left[\frac{\sum \text{peak areas of } \nu_{CO}}{\sum \text{peak areas of } \nu_{CO} \text{ at 298 K}} \right] \times 11$$

POWDER X-RAY DIFFRACTION: XRD patterns of the

supported Ru catalysts were recorded on a Rigaku MultiFlex X-ray diffractometer (Cu K$_\alpha$, λ = 1.5418 Å, 40 kV, 40 mA) with a scan rate of 2° min⁻¹, and the measurements were performed at 293-298 K under air.

X-RAY FLUORESCENCE SPECTROSCOPY (XRF): XRF was measured on a JEOL JSX-3400RII spectrometer to estimate the Ru loading on the oxide supports.

BET ANALYSIS: Nitrogen absorption was performed on a Shimadzu Micromeritics ASAP-2020 analyzer at 77 K. Samples (0.1–4.8 g) were degassed at 368 K for 4 h (SiO₂, TiO₂, K-Alu C, Ru₃₋CO/K-Alu C (K: 4 wt%, Ru: 2 wt%), and K-γ-Al₂O₃) and at 473 K for 1 h (ZnO, α-Al₂O₃, MgO, Alu C and γ-Al₂O₃) before an N₂ adsorption measurement, and the dead volume was estimated by helium.

TRANSMISSION ELECTRON MICROSCOPY: TEM images of the Ru-supported samples were taken on a JEOL JEM-3100FEF (UHR) transmission electron microscope with an acceleration voltage at 300 kV. Samples were dispersed in *n*-hexane, and the suspension was dropped onto Cu grids and dried at 293–298 K under air. Particle size distribution was estimated, assuming a spherical shape.

X-RAY ABSORPTION FINE STRUCTURE MEASUREMENTS: Ru *K*-edge XAFS spectra were measured in transmission mode at 20 K at the NW10A station of the Photon Factory Advanced Ring at KEK-IMSS (6.5 GeV, 60 mA). X-rays from the storage ring were monochromatized with a Si(311) double-crystal monochromator, and ionization chambers filled with pure Ar or Kr gas were used to monitor the incident and transmitted X-rays, respectively. Ru₃(CO)₁₂ and Ru powder were diluted with boron nitride and pelletized into a disk (10 mm in diameter) were used as Ru chemical references. All samples were enclosed in an XAFS cell sealed with two carbon caps inside a glovebox without exposure to air.

In situ Ru *K*-edge quick XAFS (QXAFS) measurements were acquired in transmission mode at the BL36XU beamline of SPring-8 (8 GeV, 100 mA). X-rays from the storage ring were monochromatized with a Si(220) channel-cut compact monochromator operated by a servomotor. Ionization chambers filled with Ar/N₂ (50/50) or pure Ar were used to monitor the incident and transmitted X-rays, respectively. A QXAFS spectrum at the Ru K-edge was recorded for 20 s (21515.89– 23438.09 eV), and a series of time-resolved QXAFS spectra were recorded every 2 min during the heating process and every 3 min at 723 K.

A Ru₃₋CO/K-Alu C sample (K: 4 wt %, Ru: 4 wt %; 180 mg) was packed into a pellet 7 mm in diameter and placed in an *in situ* XAFS cell with two Kapton film windows under N₂ (Figure S1). The cell was evacuated under vacuum at 298 K for 5 min and then the first XAFS spectrum was recorded. The temperature increased from 298 to 723 K over 1 h (7.1 K min⁻¹), which was a program similar to that used in the *in situ* FT-IR measurements. A series of QXAFS spectra was recorded during the heating process under vacuum. Finally, the sample was kept at 723 K for 5 min, and a QXAFS spectrum was recorded.

ANALYSIS OF XAFS SPECTRA: The Ru *K*-edge XAFS spectra were analyzed with IFEFFIT ver. 1.2.11 (Athena and Artemis).[70] The threshold energy was tentatively set at the inflection point of the Ru *K*-edge, and background subtraction

was performed with Autobk and the spline smoothing algorithm in Athena.[71] The energy calibration was performed by using the XAFS spectrum of Ru powder (E = 22117 eV). k^3-Weighted extended XAFS (EXAFS) oscillations (k: 30–180 nm^{-1} for Ru powder and 30–150 nm^{-1} for Ru catalysts) were Fourier transformed into R-space. Curve-fitting analysis was carried out in the R-space (0.100–0.300 nm for Ru powder, 0.105–0.320 nm for Ru$_3$(CO)$_{12}$, 0.130–0.300 nm for Ru catalysts, and 0.130–0.320 nm ($\leq$ 621 K) or 0.160–0.320 nm (> 621 K) for Ru$_3$-$_{CO}$/K-Alu C (*in situ* QXAFS)). Fitting parameters for each shell were the coordination number (CN), interatomic distance (R), Debye-Waller factor (σ^2: mean-square-displacement), and correction-of-edge energy (ΔE_0). Phase shifts and backscattering amplitudes for Ru-C(O), Ru-(C)O, Ru-Ru and Ru-O were calculated with FEFF 8 code[72-73] using structural parameters obtained from the crystal structures of Ru$_3$(CO)$_{12}$, Ru, and RuO$_2$.[74-76]

ADSORPTION OF CO: CO adsorption was performed for the Ru$_3$-$_{CO}$/K-Alu C catalysts (K: 4 wt %, Ru: 2 and 4 wt %) before they were used. The samples (1.0 g) were treated with dehydrated n-heptane (Wako Chemicals, 99.0%, 20 mL) at 343 K for 20 min under N$_2$. The solvent was removed at 293–298 K, and the sample was dried under vacuum for 30 min and kept under N$_2$.

The sample (500 mg) was enclosed in a glass reactor (volume: 46 mL) connected to a closed-batch system (volume: 118 mL), and the actual volume of the system was estimated by helium (99.999%). The system was evacuated at 293–298 K for 30 min. CO (99.95%) was admitted to the cell and the changes in CO pressure were recorded for 15 min. The amounts of adsorbed CO on the Ru catalysts were calculated from the pressure changes at 15 min.

2.3 DFT calculations

All calculations were performed with the DMol3 program[77,78] in Material Studio of Accelrys Inc. Perdew–Burke–Ernzerhof (PBE) generalized gradient functional was employed for the exchange-correlation energy. Wave functions were expanded in terms of numerical basis sets. We employed the DND basis set (double numerical basis set with the d-type polarization functions) for geometry optimization. Single-point energy calculations were performed with the larger DNP basis set (double numerical basis set with the d-type polarization functions for heavy atoms and the p-type polarization functions for hydrogen atoms). Brillouin zone integrations are performed on a Monkhorst–Pack[79] k-point grid with a k-point spacing of 0.05 Å^{-1}. The convergence criteria for electronic self-consistent iteration were set to 1.0×10^{-6} hartree. We performed geometry optimization with an orbital cutoff value of 4.3 Å and single-point energy calculations with a cutoff value of 4.7 Å.[80] The transition state was determined using the linear and quadratic synchronous transit (LST/QST) complete search method.[81] The Ru catalyst was modeled by a supercell slab that consists of a 3×3 surface unit cell with three atomic (002) surface layers. Lattice constants $a = b = 8.117$ Å) unless otherwise noted. The slab was separated by a vacuum space with a height of 15 Å. The top layer was fully relaxed, whereas the bottom two layers were fixed at the corresponding bulk positions. To confirm the

reliability of the selected model, we considered low-energy adsorption modes of acetonitrile and important reaction intermediates on the Ru surface with four and five atomic layer models, as listed in Table S3 and S4.

2.4 Nitrile hydrogenation

The catalyst (Ru 0.0396 mmol) was treated with dehydrated n-heptane (Wako Chemicals, 99.0%, 5 mL) at 343 K for 20 min under H$_2$ at atmospheric pressure (99.999%), then a mixture of a nitrile reactant (3.96 mmol) and internal standard (1.32 mmol) was added to the suspension. The molar ratio of Ru/n-octane (internal standard)/valeronitrile was 1/33/100. The amounts of Ru 2 wt % catalysts were 200 mg. Reactants, products, and the internal standard were analyzed by FID-GC (GC-17A, Shimadzu; CHIRALDEX G-DP, 0.25 mm I.D. × 30 m × 0.25 μm) at appropriate intervals. For valeronitrile hydrogenation, the calibration curves of valeronitrile (pentanenitrile), n-pentylamine, N-pentylidenepentylamine, di-n-pentylamine, and tri-n-pentylamine to the internal standard were prepared in dehydrated n-heptane.

For other nitriles, nitrile reactants and their corresponding primary amines were used for the calibration curves of GC analysis. n-Dodecane was used as an internal standard. The molar ratio of Ru/n-dodecane (internal standard)/nitrile was 1/33/100. Due to the low solubility of aromatic nitrile reactants in dehydrated n-heptane, a mixture (25 mL) of n-nonane (Wako Chemicals, 99.0%, 20 mL) and dehydrated 1,4-dioxane (Wako Chemical, 99.0%, 5 mL) was used.

Nitrile conversion and the selectivity of primary amines were calculated from the following equations.

Nitrile conversion % = $\left[\dfrac{\text{initial amount of nitrile-residual amount of nitrile}}{\text{initial amount of nitrile}}\right] \times 100$

Selectivity of primary amine % = $\left[\dfrac{\text{amount of primary amine}}{\text{amounts of all products derived from nitrile}}\right] \times 100$

After a 12 h hydrogenation reaction, the catalyst was washed with dehydrated n-heptane (5 mL × 5), and then evacuated at 293–298 K and dried under vacuum for 30 min. The dried samples were enclosed in an XAFS cell sealed with carbon caps inside a glovebox for XAFS measurements. For the TEM analysis, a sample was dispersed in n-hexane. The suspension was dropped on a Cu grid and dried at 293–298 K under air.

3. Results and discussion

3.1 *In situ* characterization of the formation of active Ru nanoparticles on K-Alu C

The adsorption of Ru$_3$(CO)$_{12}$ to the surfaces of several oxides (SiO$_2$, TiO$_2$, Al$_2$O$_3$, K-Al$_2$O$_3$, MgO etc.), the decarbonylation of the precursor, and the formation of Ru particles on the oxide surfaces have been reported in relation to catalytic CO hydrogenation, where a TiO$_2$-supported Ru catalyst was the most active for selective C$_2$-C$_4$ hydrocarbons production.[64-65] In the present study, it was found that the K-Alu C-supported Ru catalyst was the most active for the hydrogenation of nitriles among the prepared oxide-supported Ru catalysts, where small metallic Ru nanoparticles, with an

average diameter of less than 2 nm, were observed before and after the nitrile hydrogenation. Therefore, we investigated structural changes in the K-Alu C-supported Ru species (K: 4 wt %, Ru: 4 wt %) from the $Ru_3(CO)_{12}$ precursor to the active metallic Ru nanoparticles on K-Alu C by *in situ* FT-IR and *in situ* Ru *K*-edge XAFS analysis.

Figure 1 shows the Ru *K*-edge XANES spectra and EXAFS Fourier transforms of the $Ru_3(CO)_{12}$ precursor and $Ru_3(CO)_{12}$-impregnated K-Alu C. Both the XANES spectra (Figure 1a) were similar, indicating that the Ru valence states and the coordination of the precursor did not change in the K-Alu C-impregnated complex. The curve-fitting analysis of the EXAFS Fourier transforms (Figure 1c) showed the structural parameters of the coordinating carbonyl groups and the Ru-Ru interaction, and it was suggested that the Ru-CO and Ru-Ru coordination was maintained after the impregnation of the K-Alu C surface with $Ru_3(CO)_{12}$ (Table S1). Thus, there were no significant changes in the coordination framework of the $Ru_3(CO)_{12}$ precursor after it was adsorbed on the K-Alu C surface.

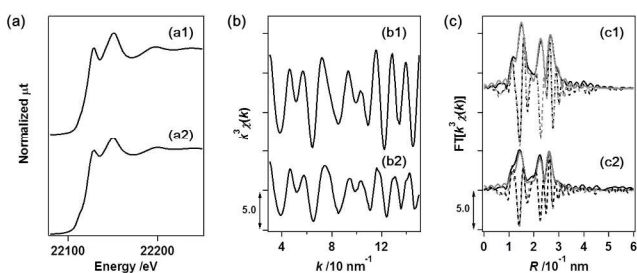**Figure 1** Ru *K*-edge XAFS spectra of (1) $Ru_3(CO)_{12}$ and (2) $Ru_{3\text{-}CO}$/K-Alu C (K: 4 wt %, Ru: 4 wt %) measured at 298 K. (a) XANES spectra, (b) k^3-weighted EXAFS oscillations, and (c) their k^3-weighted EXAFS Fourier transforms. Black and gray lines represent observed and fitted data, respectively; solid and dotted lines indicate the absolute and imaginary parts, respectively.

A series of *in situ* FT-IR spectra of $Ru_3(CO)_{12}$-impregnated K-Alu C was measured under vacuum from 298 to 723 K. The CO region is presented in Figure 2a. At 298 K, ν_{CO} peaks at 2090, 2069, 2023, 1959, and 1775 cm^{-1} were observed, and their peak intensities decreased as the temperature under vacuum increased. The linear CO ligands were released preferentially over the bridged CO groups. At 666 K, the ν_{CO} peaks almost disappeared in the FT-IR spectrum, indicating that the decarbonylation of the attached Ru complex was complete at this temperature.
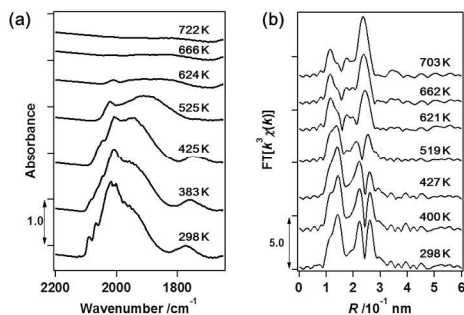
Figure 2 (a) *In situ* FT-IR spectra and (b) *in situ* Ru *K*-edge k^3-weighted EXAFS Fourier transforms of $Ru_{3\text{-}CO}$/K-Alu C (K: 4 wt %, Ru: 4 wt %) during the evacuation process.

The Ru *K*-edge EXAFS Fourier transforms changed considerably during the decarbonylation (Figure 2b). The Ru-C(O) and Ru-(C)O peaks gradually decreased, and a new peak attributed to the Ru-Ru interaction was observed at 0.267 nm. A series of *in situ* Ru *K*-edge XANES spectra and k^3-weighted EXAFS Fourier transforms of $Ru_{3\text{-}CO}$/K-Alu C obtained at temperatures from 298 to 703 K under vacuum (Figures 3a and 3b, respectively), suggested that the coordination of Ru-CO and Ru-Ru changed during the decarbonylation process. The curve-fitting analysis of the EXAFS Fourier transforms provided the CNs of Ru-C(O), Ru-(C)O, and Ru-Ru, and the Ru-Ru bond distance as a function of the temperature (Table S1). In addition to the number of remaining CO ligands estimated from the *in situ* FT-IR ν_{CO} peak areas, the CNs of Ru-CO and Ru-Ru estimated by the EXAFS curve-fitting analysis are shown in Figures 3c and 3d.

The changes in the structural parameters in Figures 3c and 3d suggested that there were three stages in the structural transformation of the supported Ru carbonyl cluster to the metallic Ru cluster on K-Alu C. In the first stage, the CN of Ru-CO and the number of remaining CO ligands began to decrease at around 400 K (Figure 3c), indicating that partial decarbonylation was initiated. The CN of Ru-Ru ($CN_{Ru\text{-}Ru}$) increased substantially, from 1 to 2–2.5, as the Ru-Ru bond distance gradually shortened (Figure 3d). These results suggest that the first partial decarbonylation promoted the nucleation of the Ru cluster on K-Alu C.

In the second stage of the structural changes, the elimination of the remaining CO ligand (decreases in the CN of Ru-CO and the ν_{CO} peak areas) continued (Figure 3c), while the change in $CN_{Ru\text{-}Ru}$ was negligible at around 450–600 K, keeping the values around 2.0–2.5 (Figure 3d). Additionally, the shortening of the Ru-Ru bond also continued with a gentle slope against the temperature during this stage. These structural changes indicate that the core of the Ru cluster approached the metallic phase with contraction of the cluster framework through the continuous release of CO ligands due to depletion of the CO ligand repulsion.
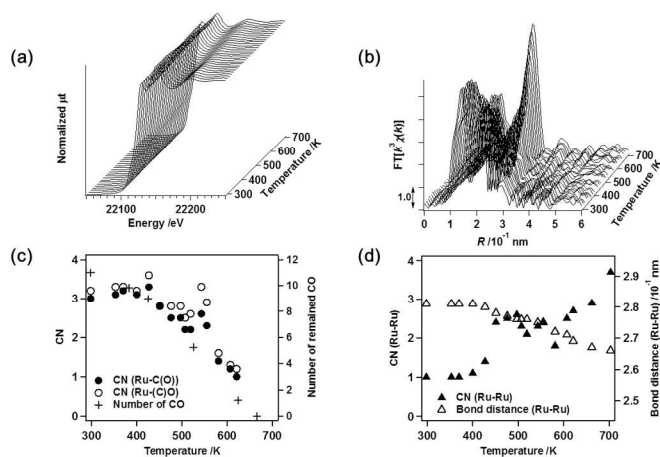
Figure 3 (a) A series of *in situ* Ru *K*-edge XANES spectra and (b) a series of *in situ* Ru *K*-edge k^3-weighted EXAFS Fourier transforms of Ru$_{3-CO}$/K-Alu C (K: 4 wt %, Ru: 4 wt %) during the evacuation from 298 to 703 K (heating rate: 7.1 K min^{-1}). (c) and (d) plots of the CNs of Ru-C(O), Ru-(C)O, and Ru-Ru, the Ru-Ru bond distance, and the number of remaining CO ligands estimated from the variation of the FT-IR ν_{CO} peak areas with temperature.

Increasing the temperature further (>600 K) completely eliminated CO ligands from the supported Ru species. Rapid increases in the CN of Ru-Ru accompanied the final elimination of CO ligands (Figure 3d). Finally, CN$_{Ru-Ru}$ reached 4, with a bond distance of around 0.266 nm, which is similar to the bond distance of Ru hexagonal close packing (hcp).[76] The final stage is the growth of the Ru cluster core into a Ru hcp cluster. Subsequent reduction with H$_2$ at 723 K completely reduced the Ru clusters to metallic Ru nanoparticles, the sizes of which depended on the loading of the Ru$_3$(CO)$_{12}$ precursor on K-Alu C (Figure 4 and Table 1).
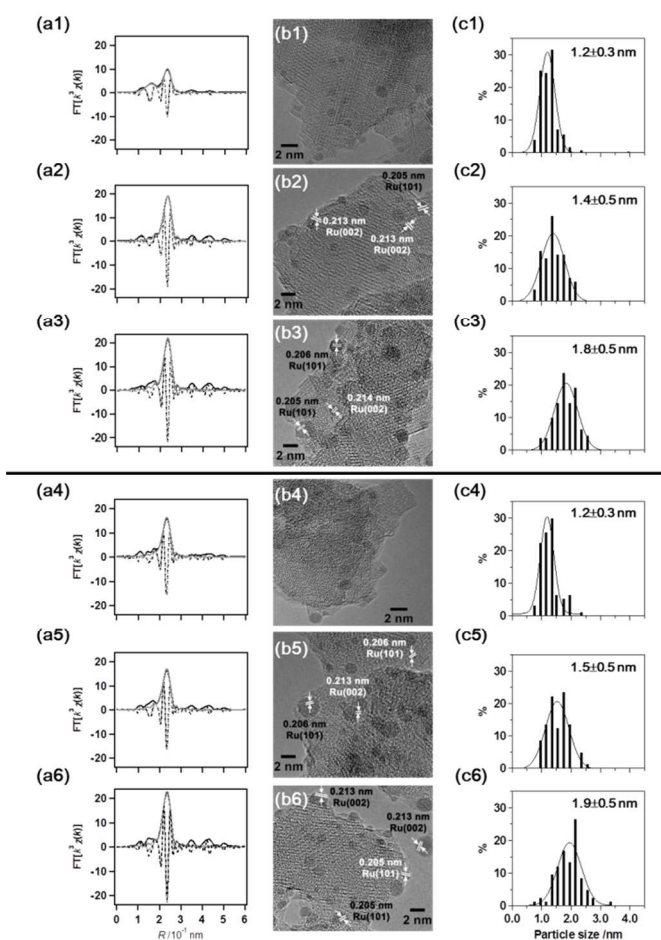

Figure 4 (a) Ru *K*-edge k^3-weighted EXAFS Fourier transforms, (b) TEM images, and (c) particle size distributions of Ru$_{3-CO}$/K-Alu C (K: 4 wt %, Ru: (1, 4) 2 wt %, (2, 5) 4 wt %, and (3, 6) 10 wt %). (1-3) Treated with dehydrated *n*-heptane at 343 K for 20 min under N$_2$. (4-6) After the hydrogenation of valeronitrile in dehydrated *n*-heptane at 343 K for 12 h. Black and gray lines on (a) represent the observed and fitted data, respectively; solid and dotted lines on (a) are absolute and imaginary parts, respectively.

The Ru *K*-edge EXAFS Fourier transforms of Ru$_{3-CO}$/K-Alu C before nitrile hydrogenation revealed that metallic Ru species were formed in the Ru loading range of 1–10 wt % (Figure 4a, Table 1, and Figure S2). The bond distance of Ru-Ru was similar to or slightly shorter than 0.267 nm, and CN$_{Ru-Ru}$ for 10 wt % Ru$_{3-CO}$/K-Alu C was estimated to be 6.5 ± 1.0 at 0.267 ± 0.001 nm. When the Ru loading was reduced, the CN$_{Ru-Ru}$ and Ru-Ru interatomic distance were reduced (Table 1). For 4 wt % Ru$_{3-CO}$/K-Alu C, CN$_{Ru-Ru}$ was 5.7 ± 0.6, with a bond distance of 0.266 ± 0.001 nm, and the CN of Ru-O was negligible. At Ru loadings lower than 2 wt %, the contribution of Ru-O was observed at around 0.20 nm, which was caused by the interaction between Ru nanoparticles and the support surface. However, the presence of direct Ru-Ru bonds at the distance of 0.265 nm suggests the feature of metallic character of Ru nanoparticles at low Ru loadings.

The particle sizes of the supported Ru species increased with the Ru loading on K-Alu C. The TEM images and estimated particle size distribution are presented in Figures 4b

and 4c. The average particle sizes before the hydrogenation were 1.2 ± 0.3, 1.4 ± 0.5, and 1.8 ± 0.5 nm for the 2, 4, and 10 wt % samples, respectively (Figure 4 (c1-c3)), where the histogram of Ru particle sizes prepared from the Ru carbonyl precursor show fairly narrow distribution. The amounts of adsorbed CO at 298 K were saturated at 0.51 and 0.29 per Ru for the 2 and 4 wt % catalysts, respectively (Figure S3), reflecting the average particle sizes of the Ru catalysts, as suggested by TEM. Although the average particle sizes increased with the increase in the Ru loading, it was less than 2 nm even on the 10 wt % catalyst, indicating that the Ru nanoparticles were dispersed and stabilized on the K-Alu C surface. In the TEM images of the 4 and 10 wt % samples, the lattice images of the (101) and (002) planes showed interplanar distances of 0.205–0.206 and 0.213–0.214 nm, respectively, which were consistent with literature interplanar distances for Ru hcp packing of 0.206 and 0.214 nm,[76] indicating the formation of metallic hcp Ru nanoparticles. Negligible peaks for Ru^0 and RuO_2 by XRD also suggested that the dispersion of the Ru nanoparticles on the K-Alu C surface was high (Figure S4). The three-stage structural transformations of the supported Ru carbonyl clusters to the metallic Ru nanoparticles on K-Alu C are summarized as reference in Figure S5. The Ru-Ru CN values (4.6 ± 0.6 and 5.7 ± 0.6, respectively) for the 2 wt % and 4 wt % Ru catalysts were much lower than the expected CN values (around 9) from the nanoparticle sizes (1.2 and 1.4 nm, respectively) estimated by the TEM images assuming a spherical shape. We propose that the small CN_{Ru-Ru} values for the 1.2–1.4 nm nanoparticles may be explained by the raft-like Ru nanocluster structures of 1-2 monolayers. The further discussion on the molecular nanocluster structures would not be valid though the comprehensive characterization was performed by *in situ* FT-IR, *in situ* Ru *K*-edge XAFS, TEM, XRD and CO adsorption, and the more detailed discussion would require further investigation.

Ru *K*-edge EXAFS and TEM analysis showed that the high dispersion of the Ru nanoparticles on K-Alu C was maintained after the hydrogenation of valeronitrile in dehydrated *n*-heptane at 343 K (Table 1 and Figure 4). The values of CN_{Ru-Ru} after the 12 h valeronitrile hydrogenation were 5.3 ± 0.8 and 6.1 ± 1.0 for the 2 and 4 wt % catalysts, respectively, and the number of Ru-O bonds was negligible for both catalysts. The average particle sizes of the 2, 4, and 10 wt % catalysts were 1.2 ± 0.3, 1.5 ± 0.5, and 1.9 ± 0.5 nm, respectively, which were similar to or slightly larger than those before the catalytic hydrogenation, although they were still less than 2 nm. Thus, on the K-Alu C surface, small, stable Ru nanoparticles with an average diameter of less than 2 nm were regulated by the stepwise structural transformations from the supported Ru_{3-CO}/K-Alu C and functioned as active catalysts for the nitrile hydrogenation.

3.2 Hydrogenation of valeronitrile on Ru catalysts

The catalytic performance of the hydrogenation of valeronitrile in dehydrated *n*-heptane in H_2 at atmospheric pressure at 343 K over various Ru catalysts is summarized in Table 2. The conversion of valeronitrile and the selectivity of the corresponding primary amine, *n*-pentylamine, were compared at the initial region of the catalytic reaction (at 90 min). The precursor $Ru_3(CO)_{12}$ was inactive for the valeronitrile hydrogenation. $Ru(acac)_3$, $[Ru(p\text{-cymene})Cl_2)]_2$, and RuO_2 were also inactive under the same reaction conditions. In contrast, the supported Ru_{3-CO}/K-Alu C (K: 4 wt %, Ru: 2 wt %) selectively formed *n*-pentylamine (31% conversion, 97% selectivity, at 90 min). The supported Ru_{3-CO}/K-Alu C catalyst did not require any basic additives like ammonia as proved by the high selectivity of the primary amine. By-product was corresponding secondary imine, and corresponding secondary amine and tertiary amine were not observed. The *n*-pentylamine selectivity on Ru_{3-CO}/K-Alu C maintained the similar value (96%) when the conversion of valeronitrile was over 99% (at 720 min) (Table 2).

PCCP

ARTICLE

Table 1 Curve-fitting results of Ru K-edge k^3-weighted EXAFS Fourier transforms of Ru$_{3\text{-CO}}$/K-Alu C (K: 4 wt %) before and after the valeronitrile hydrogenation at 343 K

Ru loading (R factor) [a]	Shell	CN	R /nm	ΔE_0 /eV	σ^2 /10^{-5} nm^2
Before the hydrogenation [b] 1 wt % (R_f = 2.3%)	Ru-O	2.1±0.6	0.201±0.002	6±4	6±2
	Ru-Ru	3.2±0.8	0.263±0.001	0±2	10±1
2 wt % (R_f = 0.8%) [c]	Ru-O	2.1±0.8	0.200±0.003	2±5	8±4
	Ru-Ru	4.6±0.6	0.265±0.001	1±1	9±1
4 wt % (R_f = 1.0%) [c]	Ru-Ru	5.7±0.6	0.266±0.001	3±1	6±1
10 wt % (R_f = 1.8%) [c]	Ru-Ru	6.5±1.0	0.267±0.001	1±2	6±1
After the hydrogenation [d] 1 wt % (R_f = 1.5%)	Ru-O	1.9±0.4	0.204±0.002	8±3	5±2
	Ru-Ru	2.5±0.5	0.263±0.001	-1±2	8±1
2 wt % (R_f = 1.9%) [e]	Ru-Ru	5.3±0.8	0.264±0.001	2±2	7±1
4 wt % (R_f = 2.6%) [e]	Ru-Ru	6.1±1.0	0.265±0.001	0±2	7±1
10 wt % (R_f = 1.7%) [e]	Ru-Ru	6.7±1.0	0.267±0.001	1±3	6±1

[a] k = 30–150 nm^{-1}, R = 0.130–0.300 nm. [b] Treated with dehydrated n-heptane at 343 K for 20 min. [c] Figure 4 (a1–a3). [d] After the valeronitrile hydrogenation in dehydrated n-heptane at 343 K for 12 h. [e] Figure 4 (a4–a6).

For comparison, we prepared Ru(acac)$_3$-impregnated K-Alu C instead of using the Ru$_3$(CO)$_{12}$ precursor (Ru$_{-\text{acac}}$/K-Alu C). Ru(acac)$_3$-impregnated K-Alu C exhibited a much lower activity for the valeronitrile hydrogenation (9% conversion, 84% selectivity, at 90 min). Corresponding secondary imine was observed as a by-product. The Ru K-edge EXAFS after the valeronitrile hydrogenation for 12 h showed differences in the local structures of the Ru species between Ru$_{3\text{-CO}}$/K-Alu C and Ru$_{-\text{acac}}$/K-Alu C (Ru: 2 wt %) (Figures 4 and S6). In the case of Ru$_{3\text{-CO}}$/K-Alu C with an averaged Ru particle size of 1.2 ± 0.3 nm, only Ru-Ru bonds at 0.264 nm were observed (CN$_{\text{Ru-Ru}}$ = 5.3 ± 0.8) (Table 1), whereas Ru-O bonds remained besides Ru-Ru bonds on Ru$_{-\text{acac}}$/K-Alu C (CN$_{\text{Ru-Ru}}$ = 2.8 ± 0.4 and CN$_{\text{Ru-O}}$ = 2.2 ± 0.5) after the hydrogenation (Table S2). The CN$_{\text{Ru-Ru}}$ and CN$_{\text{Ru-O}}$ for the Ru$_{-\text{acac}}$/K-Alu C (Ru 2 wt %) were similar to the structural parameters for Ru$_{3\text{-CO}}$/K-Alu C (Ru 1 wt %) (CN$_{\text{Ru-Ru}}$ = 2.5 ± 0.5 and CN$_{\text{Ru-O}}$ = 1.9 ± 0.4). In contrast, Ru particles with an average diameter of 2.4 ± 0.5 nm were observed in the TEM images of Ru$_{-\text{acac}}$/K-Alu C. The larger particle size and the smaller CN$_{\text{Ru-Ru}}$ than those of Ru$_{3\text{-CO}}$/K-Alu C may be controversy, which indicates that the structures of the supported Ru species on Ru$_{-\text{acac}}$/K-Alu C are a heterogeneous mixture of Ru particles and oxidized Ru species. The partial decarbonylation-promoted nucleation of Ru clusters and the subsequent stepwise formation of the Ru nanoparticles were well regulated by utilization of the Ru$_3$(CO)$_{12}$ precursor rather

than the Ru(acac)$_3$ precursor to result in the efficient formation of the active Ru nanoparticles on the K-Alu C surface.

The valeronitrile hydrogenation performance depended strongly on the type of oxide support (Table 2). For comparison, Ru$_3$(CO)$_{12}$ was supported on SiO$_2$, ZnO, TiO$_2$, MgO, γ-Al$_2$O$_3$, Alu C, γ-Al$_2$O$_3$, and K-γ-Al$_2$O$_3$ surfaces (Ru: 2 wt %) similarly to Ru$_{3\text{-CO}}$/K-Alu C. The acidic supports (e.g. SiO$_2$) and amphoteric supports (ZnO and Al$_2$O$_3$) were inactive or less active and not selective for the valeronitrile hydrogenation to n-pentylamine under identical conditions. In the cases of SiO$_2$ and γ-Al$_2$O$_3$, corresponding secondary imine was detected as a by-product. On Alu C and γ-Al$_2$O$_3$ without K, corresponding secondary amine was also observed in addition to the corresponding secondary imine as by-products. In contrast, the basic supports (MgO and K-γ-Al$_2$O$_3$) were efficient for the valeronitrile hydrogenation. Ru$_{3\text{-CO}}$/K-γ-Al$_2$O$_3$ (30% conversion, 93% selectivity, at 90 min) exhibited a similar performance to Ru$_{3\text{-CO}}$/K-Alu C. These results imply that the basic supports may increase the electron density of the supported Ru nanoparticles and suppress the unfavorable condensation reactions that form the corresponding secondary imine and amine.[23-24, 61-62]

Table 2 Conversion and selectivity of *n*-pentylamine of the valeronitrile hydrogenation on various Ru catalysts [a]

Catalyst	Conversion % [b]	*n*-Pentylamine selectivity % [c]
Ru$_3$(CO)$_{12}$	2.5	—
Ru(acac)$_3$	2.9	—
[Ru(*p*-cymene)Cl$_2$)]$_2$	2.2	—
RuO$_2$	0.1	—
K-Alu C (K: 4 wt%) [d]	1.4	—
Ru$_{3-CO}$/K-Alu C (K: 4 wt%, Ru: 2 wt %)	31 (>99) [e]	97 (96) [e]
Ru$_{-acac}$/K-Alu C (K: 4 wt%, Ru: 2 wt %)	9	84
Ru$_{3-CO}$/SiO$_2$ (Ru: 2 wt %)	8	0
Ru$_{3-CO}$/ZnO (Ru: 2 wt %)	1.9	—
Ru$_{3-CO}$/TiO$_2$ (Ru: 2 wt %)	20	47
Ru$_{3-CO}$/MgO (Ru: 2 wt %)	22	55
Ru$_{3-CO}$/α-Al$_2$O$_3$ (Ru: 2 wt %)	3	0
Ru$_{3-CO}$/Alu C (Ru: 2 wt %)	16	8
Ru$_{3-CO}$/γ-Al$_2$O$_3$ (Ru: 2 wt %)	11	1
Ru$_{3-CO}$/K-γ-Al$_2$O$_3$ (K: 4 wt%, Ru: 2 wt %)	30	93

[a] Reaction conditions: Ru = 0.0396 mmol, Ru/*n*-octane (internal standard)/valeronitrile = 1/33/100 (molar ratio), 5 mL of dehydrated *n*-heptane, 343 K, 101.3 kPa of H$_2$. [b] Nitrile conversion % = (initial amount of nitrile - residual amount of nitrile)/initial amount of nitrile × 100. At 90 min. [c] *n*-Pentylamine selectivity % = amount of *n*-pentylamine/(amount of *n*-pentylamine + amount of *N*-pentylidenepentylamine × 2 + amount of di-*n*-pentylamine × 2 + amount of tri-*n*-pentylamine × 3) × 100. At 90 min. [d] 200 mg of K-Alu C was used. [e] At 720 min.

The Ru *K*-edge EXAFS of Ru$_{3-CO}$/MgO (22% conversion, 55% selectivity, at 90 min) and Ru$_{3-CO}$/Alu C (16% conversion, 8% selectivity, at 90 min) showed that the Ru-O contribution was still present on the catalysts after the valeronitrile hydrogenation for 12 h (Table S2 and Figure S6). In particular, CN$_{Ru-Ru}$ of 2.5 ± 0.4 on Ru$_{3-CO}$/Alu C was too small, indicating that the clusterization of Ru did not proceed smoothly on the Alu C surface without K. It was reported that the electronegativities of support-metal ions changed support-metal －oxygen interactions in oxide supports, as a result, the surface oxygen atoms of basic oxide supports could nucleophilically react with decarbonylated Ru atoms with strong Ru-O (support) bonds.[64-65] The conversion of Ru$_3$(CO)$_{12}$ to active Ru nanoparticles did not reach completion on MgO and Alu C surfaces, resulting in the poor hydrogenation performance.

3.3 Effects of K and Ru loading on Alu C on the valeronitrile hydrogenation

The valeronitrile hydrogenation performance depended strongly on the loading of K on Alu C (Table 3). Ru$_{3-CO}$/K-Alu C without K was less active and selective for the *n*-pentylamine formation (8% selectivity). The selectivity of the primary amine increased with the loading of K and reached saturation at a loading of 4 wt % (97%). The basicity of Al$_2$O$_3$ can be controlled by the amount of doped K, and it becomes saturated at a K density of 13.2 nm^{-2} on Al$_2$O$_3$.[81] A K loading of 4 wt %

on Alu C corresponds to a K density of 6.3 nm^{-2}, and further doping with K did not provide significant improvements in the activity and selectivity (Table 3).

On the surface of K-Alu C with 4 wt % K, we varied the Ru loading by changing the amounts of the Ru$_3$(CO)$_{12}$ precursor and investigated the catalytic performance of the resulting catalysts for the valeronitrile hydrogenation (Table 3). The hydrogenation activity was depended on the Ru loading and the highest hydrogenation activity was observed in the Ru loading range of 2–4 wt %.

The Ru *K*-edge EXAFS and TEM analysis suggested that the average particle sizes of the supported Ru nanoparticles on K-Alu C changed with different Ru loadings (Figure 4). After the hydrogenation for 12 h, CN$_{Ru-Ru}$ were 5.3 ± 0.8, 6.1 ± 1.0, and 6.7 ± 1.0, and the average particle sizes were 1.2 ± 0.3, 1.5 ± 0.5, and 1.9 ± 0.5 nm for Ru loadings of 2, 4, and 10 wt % Ru$_{3-CO}$/K-Alu C, respectively. The decreases in the activity of Ru$_{3-CO}$/K-Alu C with a high Ru loading may be caused by the decrease in the number of surface Ru sites in the nanoparticle catalysts, although the catalyst particles were stable on Ru$_{3-CO}$/K-Alu C in the Ru loading range of 2–10 wt %.

The selectivity for *n*-pentylamine was almost constant (94–98%) for this Ru loading range, although the activity was altered by the Ru loading. The secondary imine was a by-product on the K-doped Alu C surface, and secondary amine and tertiary amine were not detected. These results indicate that the selective hydrogenation of valeronitrile to *n*-pentylamine on Ru$_{3-CO}$/K-Alu C was specific to the basic K-Alu C surface and independent of the Ru loading in the range of 1–10 wt% and the particle size of the Ru catalysts in the range less than 2 nm. The basic support surface would increase the electron density of supported Ru nanoparticles to suppress the coordination of *n*-pentylamine for the subsequent formation of the secondary imine or amine on the catalyst surface.

3.4 Hydrogenation performance for nitrile compounds on Ru$_{3-CO}$/K-Alu C

Table 4 shows the catalytic performance for the hydrogenation of nitrile compounds on Ru$_{3-CO}$/K-Alu C (K: 4 wt %, Ru: 2 wt %) at 343 K under H$_2$ at atmospheric pressure. The hydrogenation activities of aromatic nitriles were lower than that of valeronitrile, although the hydrogenation reactions reached completion after appropriate reaction times (Table 4). Selectivity for the corresponding primary amines was found to be high for the hydrogenation of benzonitrile derivatives, and corresponding secondary amines were detected as sole by-products.

Two reaction pathways of nitrile hydrogenation over SiO$_2$-supported Pt and Ru, and Raney Co have been proposed: a hydrogenated intermediate binds to a metal site with a nitrogen or an α-carbon atom, known as the M-N route and the M-C route, respectively.[18, 21, 23, 24, 27, 32, 83] In the M-N route, an imine-like nitrene intermediate is thought to form on a metal surface, forming a saturated α-carbon. This is regarded as an inactive intermediate species for the condensation reaction.[21, 23] Other intermediate species are aminocarbenes and aldimines, which
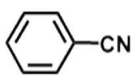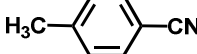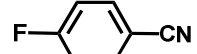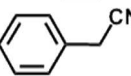
are bound to the metal site by the interaction with the π-electrons of the C=N bond or the N lone pair. These intermediates provide an unsaturated electrophilic α-carbon atom, which can nucleophilically attack higher amines.[21, 23, 83]

Table 3 Conversion and *n*-pentylamine selectivity for the valeronitrile hydrogenation on Ru$_{3\text{-CO}}$/K-Alu C [a]

K loading /wt %	Ru loading /wt %	Conversion % [b]	*n*-Pentylamine selectivity % [c]
0	2	16	8
2	2	20	27
4	2	31	97
6	2	32	98
4	1	14	94
4	1.5	24	96
4	3	27	98
4	4	28	96
4	6	25	98
4	8	20	96
4	10	20	97

[a] Reaction conditions: Ru = 0.0396 mmol, Ru/*n*-octane (internal standard)/valeronitrile = 1/33/100 (molar ratio), 5 mL of dehydrated *n*-heptane, 343 K, 101.3 kPa of H$_2$. [b] Nitrile conversion % = (initial amount of nitrile - residual amount of nitrile)/initial amount of nitrile × 100. At 90 min. [c] *n*-Pentylamine selectivity % = amount of *n*-pentylamine/(amount of *n*-pentylamine + amount of *N*-pentylidenepentylamine × 2 + amount of di-*n*-pentylamine × 2 + amount of tri-*n*-pentylamine × 3) × 100. At 90 min.

Table 4 Conversion and the selectivity of primary amines for the hydrogenation of nitriles on Ru$_{3\text{-CO}}$/K-Alu C (K: 4 wt %, Ru: 2 wt %) [a]

Entry	Reactant	Time /h	Conversion % [c]	Primary amine selectivity % [d]
1 [e]		12	> 99	96
2 [f]		82	> 99	93 [g]
3 [f]		74	> 99	96 [g]
4 [f]		85	> 99	83 [g]
5 [f]		115	> 99	70 [g]
6 [f]		114	99	95 [g]
7 [f]		127	> 99	98 [g]

[a] Reaction conditions: Ru = 0.0396 mmol, Ru/internal standard/nitrile = 1/33/100 (molar ratio), 343 K, 101.3 kPa of H$_2$. [b] Estimated from the data between 0-60 min (entry 1), 0-90 min (entries 2 and 4), 0-200 min (entry 3), 0-120 min (entry 5), or 0-150 min (entries 6 and 7). [c] Nitrile conversion % = (initial amount of nitrile - residual amount of nitrile)/initial amount of nitrile × 100. [d] Primary amine selectivity % = amount of primary amine/(amount of primary amine + amount of secondary imine × 2 + amount of secondary amine × 2) × 100. [e] Solvent: 5 mL of dehydrated *n*-heptane. Internal standard: *n*-octane. [f] Solvent: the mixture (25 mL) of *n*-nonane (20 mL) and dehydrated 1,4-dioxane (5 mL). Internal standard: *n*-dodecane. Absolute amounts of reactants and primary amines were determined by GC. [g] The ratios of products (primary amine, secondary imine, and secondary amine) were determined by ^{1}H NMR for the calculation of the selectivity.

The high selectivity of Ru$_{3\text{-CO}}$/K-Alu C for primary amines implies that nitrile compounds bound to the Ru nanoparticles via N atoms to form the corresponding nitrene species and the consequent hydrogenation at the Ru surface yielded the corresponding primary amines. This process may be positively promoted by the Ru(002) surface of the attached Ru nanoparticles, which allows electronic modification by the basic K-Alu C support efficiently. There are few examples of direct identification of the adsorbed nitrile species on catalyst surfaces, although acetonitrile and butyronitrile have been observed on Pt/Al$_2$O$_3$ by *in situ* attenuated total reflectance IR.[84-86] The vibration of nitriles has been reported to be negligible on the surface of metallic Ru species,[87] indicating the strong interaction between CN group and Ru surface. Indeed we could not observe significant peaks attributed to adsorbed CN on Ru$_{3\text{-CO}}$/K-Alu C by *in situ* FT-IR analysis.

To gain a better understanding of the selective hydrogenation performance on the Ru catalyst for primary amines, we performed periodic DFT calculations on a metallic Ru surface. Ru nanoparticle was modeled by the Ru(002) periodic slab, since the existence of this surface was observed by TEM. We investigated the adsorption of acetonitrile on the surface, which is the first reaction step of the nitrile hydrogenation. We compared the stability of each adsorbed structure by the relative potential energy based on the most stable structure, since DMol3 program we use does not support

counterpoise correction for periodic systems to remove basis set superposition error (BSSE), resulting in the overestimation of adsorption energy. The adsorbed structure whose nitrogen and carbon atoms of the CN group are coordinated at the hcp (h) and fcc (f) sites of Ru(002) surface (denoted as h-f configuration; The first term in the nomenclature represents the adsorption position of the nitrogen atom of the CN group and the second term represents the adsorption site of the carbon atom of the CN group, respectively.), respectively, was obtained as the most stable configuration, resulting in an elongated CN bond length (0.132 nm) and a bend structure with the sp^2 character of the CN bond on the surface (Figure 5a).

Other possible adsorption structures were summarized in Figure S7. When the carbon atom was displaced from the fcc (f) site to the top (t) site (from h-f configuration to h-t configuration in Figure S7), the potential energy was decreased by 3.6 kcal/mol. The nitrogen atom adsorbed preferentially at the hcp (h) site; the relative potential energies were 1.3 and 6.4 kcal/mol in the f-h and f-t configurations, respectively (Figure S7), when the nitrogen atom was displaced from the hcp (h) site to the fcc (f) site. Acetonitrile could coordinate to the Ru surface in a side-on fashion where the carbon and nitrogen atoms of the CN group were adsorbed at bridge (b) sites (Bridge (b) site locates in the middle of Ru-Ru bond in the first layer.). The whole CN group then could situate over the hcp (h) site or fcc (f) site (denoted as b-b-h and b-b-f configurations in Figure S7; The first term and the second term in the nomenclature represent the adsorption position of the nitrogen atom and the carbon atom of the CN group, respectively. The third term represents the position of the whole CN group.). The relative potential energies were 2.3 and 5.1 kcal/mol in the b-b-h and b-b-f configurations, respectively (Figure S7). When the nitrogen atom adsorbed at the top (t) site (denoted as t configuration in Figure S7), the potential energy was decreased by 9.8 kcal/mol, which was the largest decrease compared with the other configurations. The CN bond length was 0.117 nm for t configuration, which was the shortest among other configurations, indicating that acetonitrile was weakly adsorbed in the t configuration compared with the others.

Two H atoms are then transferred to the adsorbed nitrile molecule to give nitrene, carbene, or imine intermediate, as shown in Figure 5b. The nitrene species, which is formed by the saturation of the carbon atom, is proposed to be responsible for the high selectivity for primary amines because it is inactive for the condensation reaction.[21,23] On the other hand, carbene or imine intermediate involves an unsaturated electrophilic α-carbon atom, which is subject to nucleophilic attack by external primary amines to give undesired higher amines.[21, 23, 83]
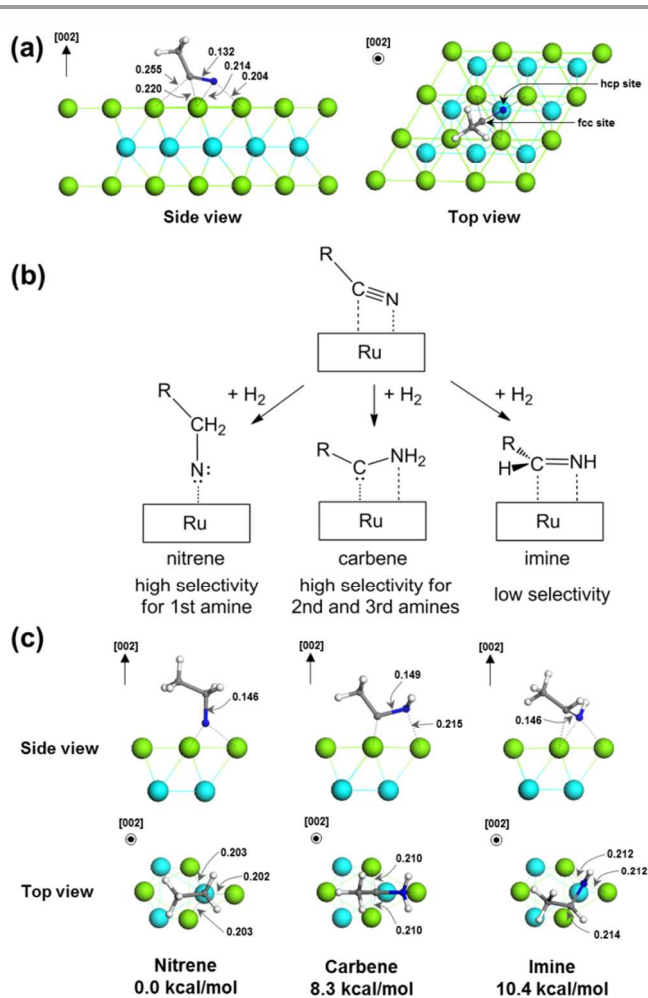

Figure 5. (a) Side and top views of the most stable adsorption structure (h-f configuration. The first term in the nomenclature represents the adsorption position of the nitrogen atom of CN group on the hcp (h) site and the second term represents the adsorption site of the carbon atom of CN group on the fcc (f) site, respectively.) of acetonitrile on the Ru surface. The C, N, H, and Ru atoms are colored in gray, blue, and white, respectively. Green and light blue spheres represent Ru atoms in the top (third) and second layers, respectively. Unit for bond distance is in nm. (b) Possible reaction pathways of nitrile hydrogenation on the Ru catalyst. (c) Side and top views of nitrene, carbene, and imine intermediates on the Ru surface, and relative potential energies against nitrene intermediates (0.0 kcal/mol). Unit for bond distance is in nm.

DFT calculations showed that the formation of the nitrile intermediate is the most favored on the Ru surface (Figure 5); the relative potential energy of the nitrene intermediate was much lower than those of carbene (8.3 kcal/mol) and imine (10.4 kcal/mol) intermediate. The nitrogen atom of the nitrene species was located on the hcp (h) site of the Ru(002) surface, and the migration of the nitrogen atom to the fcc (f) site is found to be endothermic (5.0 kcal/mol). The strong bonding of the nitrogen atom of the nitrene species to the Ru surface increased the stability of the nitrene intermediate species preferable for the selective hydrogenation to primary amines.

We explored a possible reaction pathway for the hydrogenation of acetonitrile to the nitrene intermediate, as shown in Figure S8. An H atom adsorbed over an fcc (f) site on the Ru catalyst surface and approached to the carbon atom of

adsorbed acetonitrile via transition state 1, forming a monohydrogenated species. The monohydrogenated species was adsorbed on the Ru surface with the carbon atom on the top (t) site and the nitrogen atom on the hcp (h) site. The first hydrogenation process was found to be exothermic by −7.2 kcal/mol with an activation barrier of 15.2 kcal/mol. Then the monohydrogenated species produced the corresponding amine via transition state 2. The second hydrogenation process proceeded with a little lower barrier of 14.1 kcal/mol. The DFT study shows that Ru has the intrinsic nature of producing a favourable reaction pathway from nitrile species to primary amine species. Although the current DFT calculation does not include the effect of supports, the obtained results would offer an insight into the high primary amine selectivity on the Ru_{3-CO}/K-Alu C catalyst.

4. Conclusions

The stepwise reaction processes of Ru nanoparticle formation from $Ru_3(CO)_{12}$ on a basic K-doped Alu C surface were identified by *in situ* FT-IR and *in situ* Ru *K*-edge XAFS analysis. The partial decarbonylation initiated the nucleation of the Ru cluster core on the surface, and the core approached the Ru metallic phase while continuously releasing CO. Finally, stable metallic Ru nanoparticles with an average particle size of less than 2 nm were formed on the K-Alu C surface. The Ru nanoparticle catalysts on K-Alu C were active for the hydrogenation of nitrile derivatives and exhibited high selectivity for the corresponding primary amines. It was demonstrated by DFT calculations that the Ru surface activated nitriles in such a way that the formation of primary amines would be favourable via a nitrene-like intermediate structure. Thus, it might be stated that the basic support would provide the selective formation of active Ru nanoparticles that would be advantageous to the selective reaction pathways for nitrile hydrogenation to primary amines.

.

Notes and references

1. H. Greenfield, *Ind. Eng. Chem. Prod. Res. Dev.* 1967, **6,** 142.
2. S. Gomez; J. A. Peters; T. Mashmeyer, *Adv. Synth. Catal.* 2002, **344,** 1037.
3. A. Infantes-Molina; J. Mérida-Robles; P. Braos-García; E. Rodríquez-Castellón; E. Finocchio; G. Busca ; P. Maireles-Torres; A. Jiménez-López, *J.Catal.* 2004, **225,** 479.
4. S. Gomez; J. Peters; J. van der Waal; W. Zhou; T. Maschmeyer, *Catal. Lett.* 2002, **84,** 1.
5. J. L. Klinkenberg; J. F. Hartwig, *Angew. Chem., Int. Ed.* 2011, **50,** 86.
6. C. de Bellefon; P. Fouilloux, *Catal. Rev.: Sci. Eng.* 1994, **36,** 459.
7. X. Ye; P. N. Plessow; M. K. Brinks; M. Schelwies; T. Schaub; F. Rominger; R. Paciello; M. Limbach; P. Hofmann, *J. Am. Chem. Soc.* 2014, **136,** 5923.
8. C. Gunanathan; D. Milstein, *Angew. Chem., Int. Ed.* 2008, **47,** 8661.
9. S. Das; S. Zhou; D. Addis; S. Enthaler; K. Junge; M. Beller, *Top. Catal.* 2010, **53,** 979.
10. S. Enthaler; K. Junge; D. Addis; G. Erre; M. Beller, *ChemSusChem* 2008, **1,** 1006.
11. Y. Huang; W. M. H. Sachtler, *J. Catal.* 1999, **188,** 215.
12. P. Kukula; K. Koprivova, *J. Catal.* 2005, **234,** 161.
13. P. Kukula; M. Studer; H.-U. Blaser, *Adv. Synth. Catal.* 2004, **346,** 1487.
14. C. Gunanathan; M. Hölscher; W. Leitner, *Eur. J. Inorg. Chem.* 2011, **2011,** 3381.
15. D. J. Segobia; A. F. Trasarti; C. R. Apestequia, *Appl. Catal., A.* 2012, **445-446,** 69.
16. Y. Huang; W. M. H. Sachtler, *Appl. Catal., A.* 1997, **163,** 245.
17. L. Hegedűs; T. Máthé; T. Kárpáti, *Appl. Catal., A.* 2008, **349,** 40.
18. P. Schärringer; T. E. Müller; J. A. Lercher, *J. Catal.* 2008, **253,** 167.
19. M. Chatterjee; M. Sato; H. Kawanami; T. Yokoyama; T. Suzuki; T. Ishizaka, *Adv. Synth. Catal.* 2010, **352,** 2394.
20. H. Li; Y. Wu; J. Zhang; W. Dai; M. Qiao, *Appl. Catal., A.* 2004, **275,** 199.
21. J. Krupka; J. Pasek, *Curr. Org. Chem.* 2012, **16,** 988.
22. Y. Huang; W. M. H. Sachtler, *Appl. Cata., A.* 1999, **182,** 365.
23. A. Chojecki; H. Jobic; A. Jentys; T. Müller; J. Lercher, *Catal. Lett.* 2004, **97,** 155.
24. A. Chojecki; M. Veprek-Heijman; T. E. Müller; P. Schärringer; S. Veprek; J. A. Lercher, *J. Catal.* 2007, **245,** 237.
25. H. S. Kim; S. H. Seo; H. Lee; S. D. Lee; Y. S. Kwon; I.-M. Lee, *J. Mol. Catal. A: Chem.* 1998, **132,** 267.
26. Y. Huang; V. Adeeva; W. M. H. Sachtler, *Appl. Catal., A.* 2000, **196,** 73.
27. Y. Huang; W. M. H. Sachtler, *J. Catal.* 1999, **184,** 247.
28. P. Gai; K. Kourtakis; E. D. Boyes, *Catal. Lett.* 2005, **102,** 1.
29. A. Nieto-Márquez; D. Toledano; P. Sánchez; A. Romero; J. L. Valverde, *J. Catal.* 2010, **269,** 242.
30. S. Werkmeister; K. Junge; B. Wendt; A. Spannenberg; H. Jiao; C. Bornschein; M. Beller, *Chem. –Eur. J.* 2014, **20,** 4227.
31. S. Takemoto; H. Kawamura; Y. Yamada; T. Okada; A. Ono; E. Yoshikawa; Y. Mizobe; M. Hidai, *Organometallics* 2002, **21,** 3897.
32. Y. Huang; W. M. H. Sachtler, *J. Catal.* 2000, **190,** 69.
33. R. Reguillo; M. Grellier; N. Vautravers; L. Vendier; S. Sabo-Etienne, *J. Am. Chem. Soc.* 2010, **132,** 7854.
34. H. Kusaka; Y. Hara; M. Onuki; T. Akai; M. Okuda, *J. Catal.* 1996, **161,** 96.
35. F. Hochard; H. Jobic; J. Massardier; A. J. Renouprez, *J. Mol. Catal. A: Chem.* 1995, **95,** 165.
36. F. Medina; R. Dutartre; D. Tichit; B. Coq; N. T. Dung; P. Salagre; J. E. Sueiras, *J. Mol. Catal. A: Chem.* 1997, **119,** 201.

37. P. Braos-García; P. Maireles-Torres; E. Rodríguez-Castellón; A. Jiménez-López, *J. Mol. Catal. A: Chem.* 2003, **193,** 185.
38. M. Arai; T. Ebina; M. Shirai, *Appl. Surf. Sci.* 1999, **148,** 155.
39. C. V. Rode; M. Arai; Y. Nishiyama, *J. Mol. Catal. A: Chem.* 1997, **118,** 229.
40. M. C. Carrión; B. R. Manzano; F. A. Jalón; I. Fuentes-Perujo; P. Maireles-Torres; E. Rodríguez-Castellón; A. Jiménez-López, *Appl. Catal., A.* 2005, **288,** 34.
41. M. H. S. A. Hamid; C. L. Allen; G. W. Lamb; A. C. Maxwell; H. C. Maytum; A. J. A. Watson; J. M. J. Williams, *J. Am. Chem. Soc.* 2009, **131,** 1766.
42. K. Yamaguchi; J. He; T. Oishi; N. Mizuno, *Chem. –Eur. J.* 2010, **16,** 7199.
43. J. W. Kim; K. Yamaguchi; N. Mizuno, *J. Catal.* 2009, **263,** 205.
44. J. He; J. W. Kim; K. Yamaguchi; N. Mizuno, *Angew. Chem., Int. Ed.* 2009, **48,** 9888.
45. R. García-Álvarez; J. Díez; P. Crochet; V. Cadierno, *Organometallics* 2011, **30,** 5442.
46. T. Oshiki; H. Yamashita; K. Sawada; M. Utsunomiya; K. Takahashi; K. Takai, *Organometallics* 2005, **24,** 6287.
47. J. W. Kim; K. Yamaguchi; N. Mizuno, *Angew. Chem.* 2008, **120,** 9389.
48. S.-I. Murahashi; T. Naota; H. Taki; M. Mizuno; H. Takaya; S. Komiya; Y. Mizuho; N. Oyasato; M. Hiraoka; M. Hirano, *J. Am. Chem. Soc.* 1995, **117,** 12436.
49. K.-N. T. Tseng; A. M. Rizzi; N. K. Szymczak, *J. Am. Chem. Soc.* 2013, **135,** 16352.
50. K. Yamaguchi; N. Mizuno, *Angew. Chem., Int. Ed.* 2003, **42,** 1480.
51. T. Oishi; K. Yamaguchi; N. Mizuno, *Top. Catal.* 2010, **53,** 479.
52. J. He; K. Yamaguchi; N. Mizuno, *J. Org. Chem.* 2011, **76,** 4606.
53. T. Oishi; K. Yamaguchi; N. Mizuno, *Angew. Chem., Int. Ed.* 2009, **48,** 6286.
54. M. Kotani; T. Koike; K. Yamaguchi; N. Mizuno, *Green Chem.* 2006, **8,** 735.
55. N. Mizuno; K. Yamaguchi, *Catal. Today* 2008, **132,** 18.
56. J. W. Kim; J. He; K. Yamaguchi; N. Mizuno, *Chem. Lett.* 2009, **38,** 920.
57. K. Yamaguchi; J. W. Kim; J. He; N. Mizuno, *J. Catal.* 2009, **268,** 343.
58. F. Nikaidou; H. Ushiyama; K. Yamaguchi; K. Yamashita; N. Mizuno, *J. Phys. Chem. C* 2010, **114,** 10873.
59. J. W. Kim; T. Koike; M. Kotani; K. Yamaguchi; N. Mizuno, *Chem. – Eur. J.* 2008, **14,** 4104.
60. K. Yamaguchi; T. Koike; J. W. Kim; Y. Ogasawara; N. Mizuno, *Chem. –Eur. J.* 2008, **14,** 11480.
61. F. M. Cabello; D. Tichit; B. Coq; A. Vaccari; N. T. Dung, *J. Catal.* 1997, **167,** 142.
62. M. J. F. M. Verhaak; A. J. van Dillen; J. W. Geus, *Catal. Lett.* 1994, **26,** 37.
63. A. C. Gluhoi; P. Mărginean; U. Stănescu, *App. Catal., A.* 2005, **294,** 208.
64. K. Asakura; K.-K. Bando; Y. Iwasawa, *J. Chem. Soc., Faraday Trans.* 1990, **86,** 2645.
65. K. Asakura; Y. Iwasawa, *J. Chem. Soc., Faraday Trans.* 1990, **86,** 2657.
66. C. Ortiz-Cervantes; I. Iyañez; J. J. García, *J. Phys. Org. Chem.* 2012, **25,** 902.
67. A. B. Pangborn; M. A. Giardello; R. H. Grubbs; R. K. Rosen; F. J. Timmers, *Organometallics* 1996, **15,** 1518.
68. B. F. G. Johnson; J. Lewis; P. R. Raithby; G. Süss, *J. Chem. Soc., Dalton Trans.* 1979, 1356.
69. K. Asakura; M. Yamada; Y. Iwasawa; H. Kuroda, *Chem. Lett.* 1985, **14,** 511.
70. M. Newville; B. Ravel; D. Haskel; J. J. Rehr; E. A. Stern; Y. Yacoby, *Phys. B* 1995, **208–209,** 154.
71. B. Ravel; M. Newville, *J. Synchrotron Radiat.* 2005, **12,** 537.
72. A. L. Ankudinov; A. I. Nesvizhskii; J. J. Rehr, *Phys. Rev. B* 2003, **67,** 115120.
73. M. S. Moreno; K. Jorissen; J. J. Rehr, *Micron* 2007, **38,** 1.
74. C. Boman, *Acta. Chem. Scand.* 1970, **24,** 116.
75. M. R. Churchill; F. J. Hollander; J. P. Hutchinson, *Inorg. Chem.* 1977, **16,** 2655.
76. E. O. Hall; J. Crangle, *Acta Crystallogr.* 1957, **10,** 240.
77. B. Delley, *J. Chem. Phys.* 1990, **92,** 508.
78. B. Delley, *J. Chem. Phys.* 2000, **113,** 7756.
79. H. J. Monkhorst,; J. D. Pack, *Phys. Rev. B.* 1976, **13,** 5188.
80. V. A. Basiuk; L. V. Henao-Holguín, *J. Comput. Theor. Nanos.* 2013, **10,** 1266.
81. N. Govind; M. Petersen; G. Fitzgerald; D. King-Smith; J.Andzelm, *Comp. Mat. Sci.* 2003, **28,** 250.
82. A. Iordan; M. I. Zaki; C. Kappenstein, *J. Chem. Soc., Faraday Trans.* 1993, **89,** 2527.
83. J. Krupka; J. Drahonsky; A. Hlavackova, *React. Kinet., Mech. Catal.* 2013, **108,** 91.
84. I. Ortiz-Hernandez; D. J. Owens; M. R. Strunk; C. T. Williams, *Langmuir* 2006, **22,** 2629.
85. I. Ortiz-Hernandez; C. T. Williams, *Langmuir* 2003, **19,** 2956.
86. I. Ortiz-Hernandez; C. T. Williams, *Langmuir* 2007, **23,** 3172.
87. O. M. Oranskaya; I. V. Semenskaya; V. N. Filimonov, *React. Kinet. Catal. Lett.* 1976, **5,** 135.